# *Chapter-5*

## *Site engineering: A Tool to Enhance Functional Properties in High-Temperature Lead-Free Relaxors Prepared via Air Quenching*

# Chapter 5
# Site engineering: A Tool to Enhance Functional Properties in High-Temperature Lead-Free Relaxors Prepared via Air Quenching

## 5.1 Introduction

The increasing demand for eco-friendly and energy-efficient electronic devices has driven the development of lead-free piezoelectric perovskite materials as an alternative to traditional lead-based materials[65], [240]. As elaborated in Chapter 1, among various lead-free ferroelectrics, Bismuth Ferrite, $BiFeO_3$ (BFO) and Barium Titanate, $BaTiO_3$ (BT) are two well-known ferroelectric materials that have shown promise as lead-free alternatives [43]. BFO is notable for exhibiting high Curie temperature ~830 ℃ and an antiferromagnetic Neel temperature of 370 ℃ while BT is recognized for its high dielectric constant. The versatile nature of BFO allows for the creation of a diverse range of devices, which can harness a single functionality, such as ferroelectricity, piezoelectric response, or birefringence, or combine multiple functionalities synergistically, such as through the magnetoelectric effect [241]. Additionally, apart from its multiferroic properties encompassing both ferroelectricity and ferromagnetism, $BiFeO_3$ exhibits a band gap ranging from 2.6 eV to 3 eV, originating from electronic transitions within the Fe 3d orbitals [241]. On the other hand, $BaTiO_3$, a ferroelectric material, possesses a high dielectric constant and a band gap in the ultraviolet range (3.2 eV to 3.4 eV) due to electronic transitions involving the Ti 3d orbitals [242].

The solid solution of BF-BT offers appealing characteristics for high temperature applications owing to high $T_C$, improved piezoelectric charge coefficient ($d_{33}$) and multiferroic nature [11]. However, their functional properties such as dielectric and ferroelectric properties can be improved further to make them viable for variety of practical applications. The band structure and band gap of the material, along with other electrical properties, can be influenced by the formation of a solid solution between BFO and BT. However, achieving pure phase formation

in BFO-based compositions can be challenging due to Bi volatilization during high-temperature heat treatments which causes charge imbalance. The reduction of $Fe^{3+}$ to $Fe^{2+}$ along with oxygen vacancies leads to increased conductivity henceforth deteriorating overall dielectric and ferroelectric properties, making them unsuitable for certain applications [182], [243]. To address this issue, several techniques have been proposed to enhance the functional properties of these materials, including doping with various elements, using different synthesis methods, and modifying the crystal structure. Air quenching have been proved to be effective in enhancing the resistivity and reducing the dielectric losses [110], [199].

Site engineering, as a novel technique for controlling the atomic positions of constituent ions in a crystal lattice, has emerged as a promising technique for improving the functional properties of various materials, including ferroelectrics. The technique involves changing the positions of specific ions in the crystal lattice to achieve the desired properties. This technique has been successfully used to enhance the functional properties of various materials, including ferroelectrics [3]. Chemical modification via rare earth or alkaline earth elements at A, B or both sites and addition of $ABO_3$ type end members as solid solution have proven to be an effective method to achieve pure phase formation, suppress leakage current density and enhance functionality [182], [182], [191], [191], [196], [221], [243], [244], [244], [245].

In this chapter, we explicitly explore the use of site engineering to enhance the functional properties by comparing two differently modified high-temperature lead-free $BiFeO_3$-$BaTiO_3$ relaxors prepared via air quenching. The aim of this comparative study is to investigate the effect of site engineering on the dielectric, ferroelectric, and optical properties of two differently modified systems with substitution at A and B site in $BiFeO_3$-$BaTiO_3$ relaxors. The objective is to determine the optimal conditions for achieving improved functional properties and to provide insights into the mechanism of site engineering in $BiFeO_3$-$BaTiO_3$ relaxors.

## 5.2 Experimental Details

As discussed in detail in Chapter 3 and Chapter 4, two different binary solid solutions of $0.67BiFe_{0.97-x}Ga_{0.03}Sc_xO_3$-$0.33BaTiO_3$ abbreviated as BFSBT-x where x indicates the concentration and $0.67Bi_{1-y}La_yFeGaO_3$-$0.33BaTiO_3$ abbreviated as BLFBT-y where y indicates the particular concentration and combinedly x, y ≤ 0.07 were prepared using conventional solid-state method utilizing air quenching technique. The stoichiometric amount of AR grade oxide powders of $Fe_2O_3$, $Bi_2O_3$, $Ga_2O_3$, $Sc_2O_3$, $BaCO_3$, $TiO_2$ and $La_2O_3$ with assay ≥ 99% were immersed in ethanol solvent and ball milled for 24 hours using high energy planetary ball mill (Retsch PM400, Germany). 5 mol% extra $Bi_2O_3$ was incorporated to compensate for Bi volatility. The calcination of the obtained powders was done at 850 ºC for 2 hours. Subsequently, 2 wt. % polyvinyl alcohol (PVA, which acts as binder) was added to calcined powder and pressed into disk pellets with 10 mm diameter using uniaxial hydraulic press. After burning out the PVA at 550 ℃ the green pellets were sintered for two hours at 960 ℃ for BFSBT-x and 980 ℃ for BLFBT-y. The sintered pellets were polished and then electroded by applying silver paste followed by firing at 500 ℃ for 30 min. The dc poling was done by applying the field of about 4 kV/mm for 30 minutes at 80 ℃ to the electroded pellet immersed in silicone oil.

The crystal structural characterization of the prepared samples was done using benchtop X-ray diffractometer (Rigaku Miniflex 600, Japan) and 5 kW SmartLab rotating anode (Cu) Rigaku diffractometer with a 2θ step size of 0.02º at a scan rate of 1 º/min. Further, to evaluate the temperature-dependent (30 ºC – 500 ºC) dielectric properties of the samples in the frequency range 20 Hz to 10 MHz, Keysight's E4990A impedance analyzer was used. The measurement for ferroelectric properties was done using Precision Premier II, Radiant Technology's ferroelectric loop tracer. The UV-vis characterization was conducted using UV-VIS

Spectrophotometer (UV-2600 Shimadzu) in diffuse reflectance mode for the band gap analysis, covering a wavelength range of 200-800 nm.

## 5.3 Results and Discussion

### 5.3.1 Crystal Structure Analysis

The phase formation of the prepared bulk ceramics was performed using XRD characterization. The typical X-ray diffraction (XRD) patterns of BFSBT-x and BLFBT-y with various concentration of x, $y \leq 0.07$ at room temperature are illustrated in Figure 5.1 (a) and Figure 5.1(b) respectively. Pure perovskite structure was confirmed for all samples. A peak observed in the region $2\theta \sim 25^{o}$ - $29^{o}$ in the lower concentration compositions of BFSBT in Figure 5.1 (a) corresponds to $Bi_{25}Fe_4O_{39}$ or $Bi_2Fe_4O_9$ secondary phases appeared due to volatization of $Bi_2O_3$ during high temperature heat treatment [182], [185], [246]. However, no detectable impurity was observed in BLFBT, suggesting co-doping can inhibit secondary phase formation. Absence of clear peak splitting of the peaks around $39^{o}$ and $45^{o}$ indicates psuedocubic phase structure. The XRD peaks in Figure 5.1 are indexed according to pseudocubic phase structure. The detailed Rietveld refinement studies of these samples are already discussed in Chapter 3 and Chapter 4. From the analysis we obtained the Ti/Fe-O bond lengths to be 1.8629 Å (x=0.01), 1.8742 Å (x=0.03), 1.8644 Å (x=0.05) and 1.8756 Å (x=0.07) for BFSBT-x and 1.8989 Å (y=0.01), 1.8921 Å (y=0.03), 1.8948 Å (y=0.05) and 1.9000 Å (y=0.07) for BLFBT-y. The variation in the bond lengths follows the opposite trends for BFSBT-x and BLFBT-y up to x, $y \leq 0.05$ and above this concentration both increases irrespective of site.

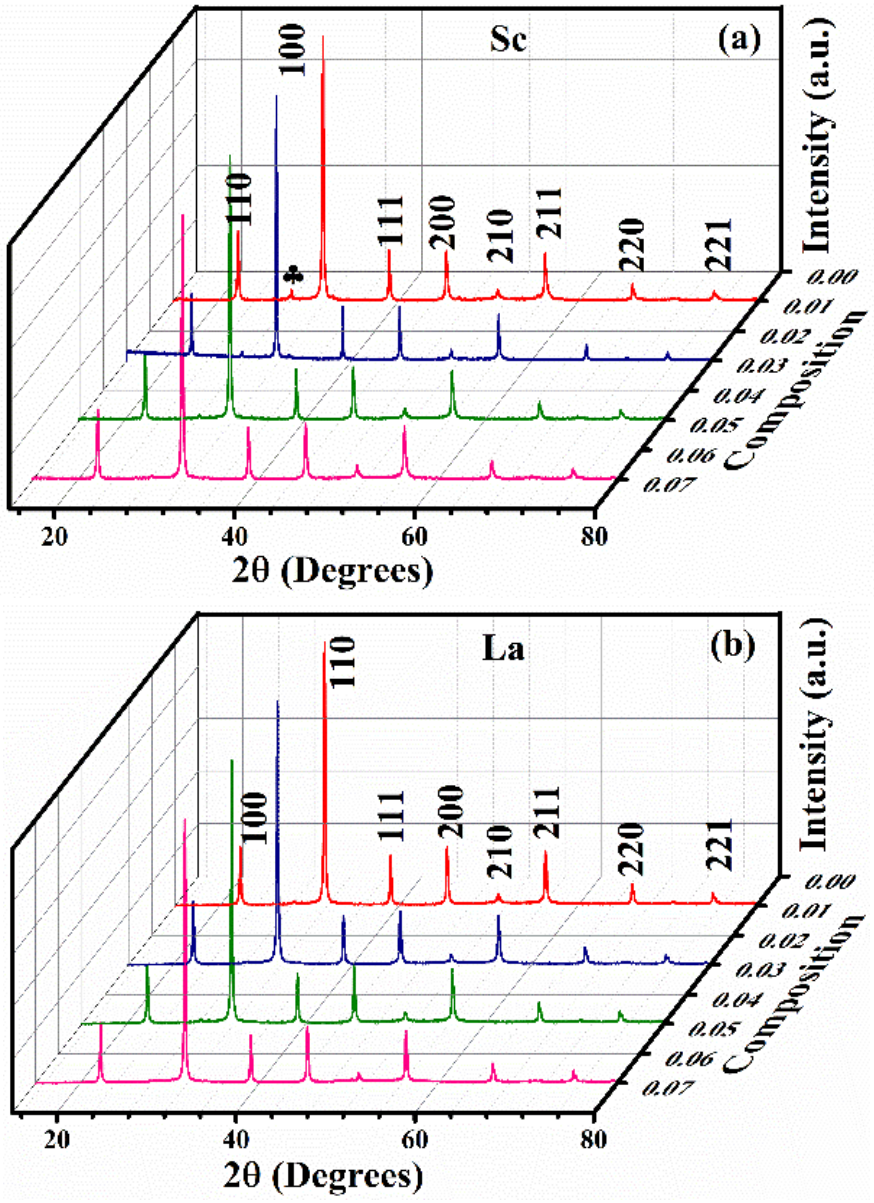


Figure 5.1 The XRD patterns of various compositions for (a) BFSBT-x and (b) BLFBT-y ceramics.

### 5.3.2 Study of Optical Properties

In this chapter, we examined the optical properties and band gap variations in doped BFSBT-x and BLFBT-y solid solutions, leveraging data from UV-Vis DRS and Kubelka-Munk Tauc plots. The optical band gap is a crucial property of materials, defining the minimum energy required for electron excitation from the valence band to the conduction band, resulting in light absorption at specific wavelengths. The band structure and band gap of the material,

along with other electrical properties, can be influenced by the formation of a solid solution between BFO and BT. In BFO, the valence band arises from the hybridization of Fe 3d and O 2p orbitals, while the conduction band is formed by unoccupied Fe 3d orbitals. In contrast, in BT, the valence and conduction bands result from the combination of Ti 3d and O 2p orbitals. The atomic-level mixing of BFO and BT in a solid solution alters the hybridization of Fe 3d, Ti 3d, and O 2p orbitals. Figure 5.2 depicts the absorbance spectra obtained from UV-Vis diffuse reflectance spectroscopy (DRS). The energy band gap of a material was calculated using Kubelka Munk Function and the Tauc plot method.

The Kubelka-Munk function F(R) is defined as:

$$F(R) = (1 - R)^2/2R \qquad (5.1)$$

where R is the reflectance of the sample. F(R) is proportional to the absorbance (A) and can be used as an approximation for the absorption coefficient (α) of the material. The relationship is given by:

$$F(R) \approx \alpha \qquad (5.2)$$

The Kubelka Munk plot is a linear plot of $(F(R)h\nu)^n$ versus photon energy (hν) used to estimate the band gap ($E_g$) of the material from the absorption data. It assumes that the absorption coefficient is proportional to $(h\nu - E_g)$ as shown in given equation:

$$(F(R)h\nu)^n = A(h\nu - E_g) \qquad (5.3)$$

where α is the absorption coefficient (approximated by (F(R)), hν is the photon energy, $E_g$ is the band gap energy, A is a constant and n depends on the nature of the electronic transition (n = 1/2 for indirect allowed transitions, n = 2 for direct allowed transitions).

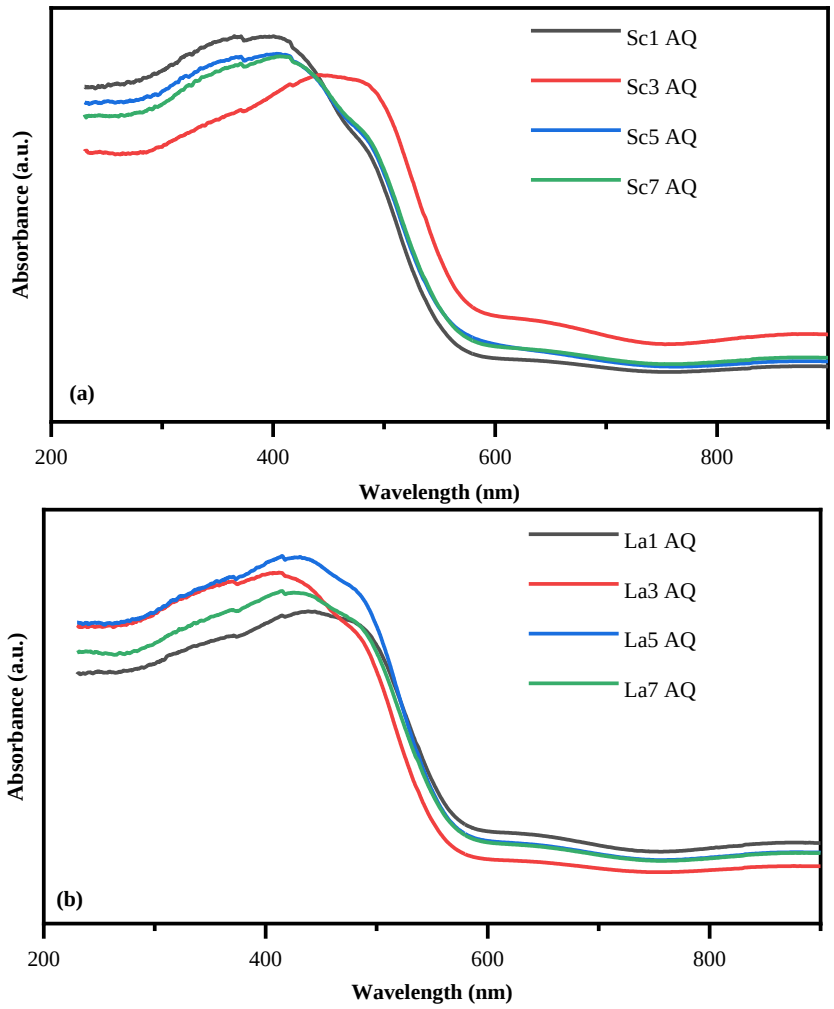


Figure 5.2 (a) UV-Vis diffuse reflectance spectroscopy (UV-Vis DRS) spectra of (a) BFSBT-x and (b) BLFBT-y where x, y ≤ 0.07.

The Kubelka Munk plot for BFSBT-x and BLFBT-y are depicted in Figure 5.3 and Figure 5.4, respectively. The analysis reveals significant impacts of doping on the electronic structure of these materials, as evidenced by varying band gap energies at different doping levels of Sc and La. The BFSBT-x series shows a reduction in the band gap from 1.95 eV at 1 mol% to 1.81 eV at 3 mol%, followed by a slight increase and stabilization around 1.88-1.89 eV at higher concentrations (5 and 7 mol%). This trend suggests modifications in the local electronic environment, potentially through alterations in the Ti/Fe-O bond character and the overall

electronic band structure. Conversely, The BLFBT-y series displays a non-monotonic band gap variation, with initial values starting at 1.80 eV for 1 mol%, peaking at 1.93 eV for 3 mol%, and subsequently decreasing slightly. This indicates that La, which likely substitutes at A-sites, affects the lattice differently due to its larger ionic radius compared to Bi, impacting the lattice strain and the orbital overlap between atoms. The trend for the $E_g$ on increasing the doping concentration is just opposite to the trend obtained for Ti/Fe-O bond length variation in both the cases suggesting the correlation of octahedral distortion and bandgap of the material. Additionally, the crystal structure's impact on optical properties is profound. Doping at A and B sites influences the octahedral tilting and bond lengths, directly affecting the band structure and optical band gaps. A-site doping primarily alters lattice parameters and volume, influencing electronic bandwidth through changes in Bi-O or La-O interactions. B-site doping, such as with Sc, directly impacts the octahedra bond character, modifying the positions of the conduction and valence bands. Having stated that the trend for $E_g$ with respect to doping concentration is just opposite in BFSBT and BLFBT for x, $y \leq 0.05$, attributable to different site engineering involved. The bandgap falls in visible range and has decreased for both type of doping with respect to BFO and BT.

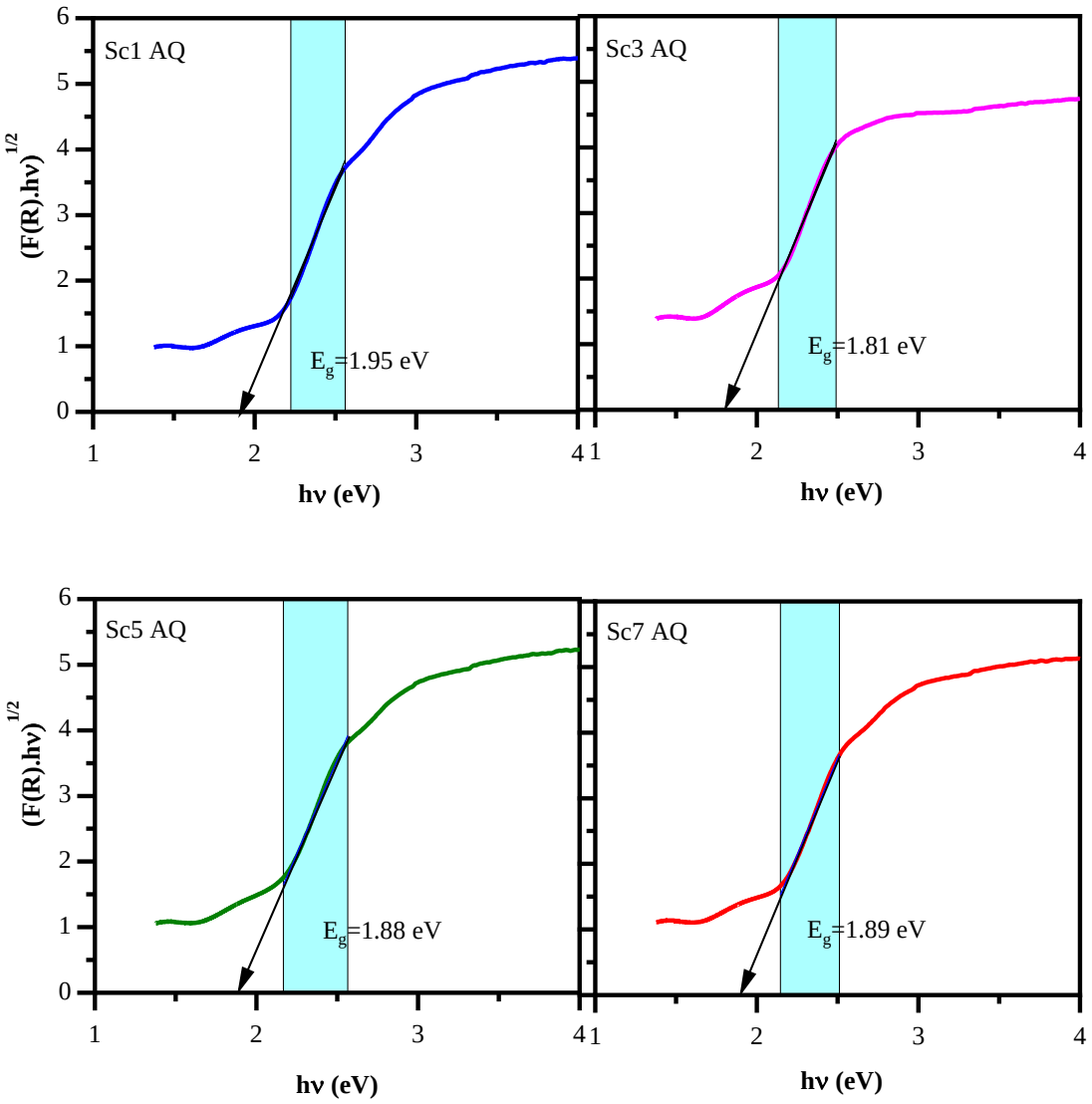


Figure 5.3 Kubelka Munk Tauc plot for BFSBT-x with (a) x=0.01 (Sc1), (b) x=0.03 (Sc3), (c) x=0.05 (Sc5), and (d) x=0.07 (Sc7).

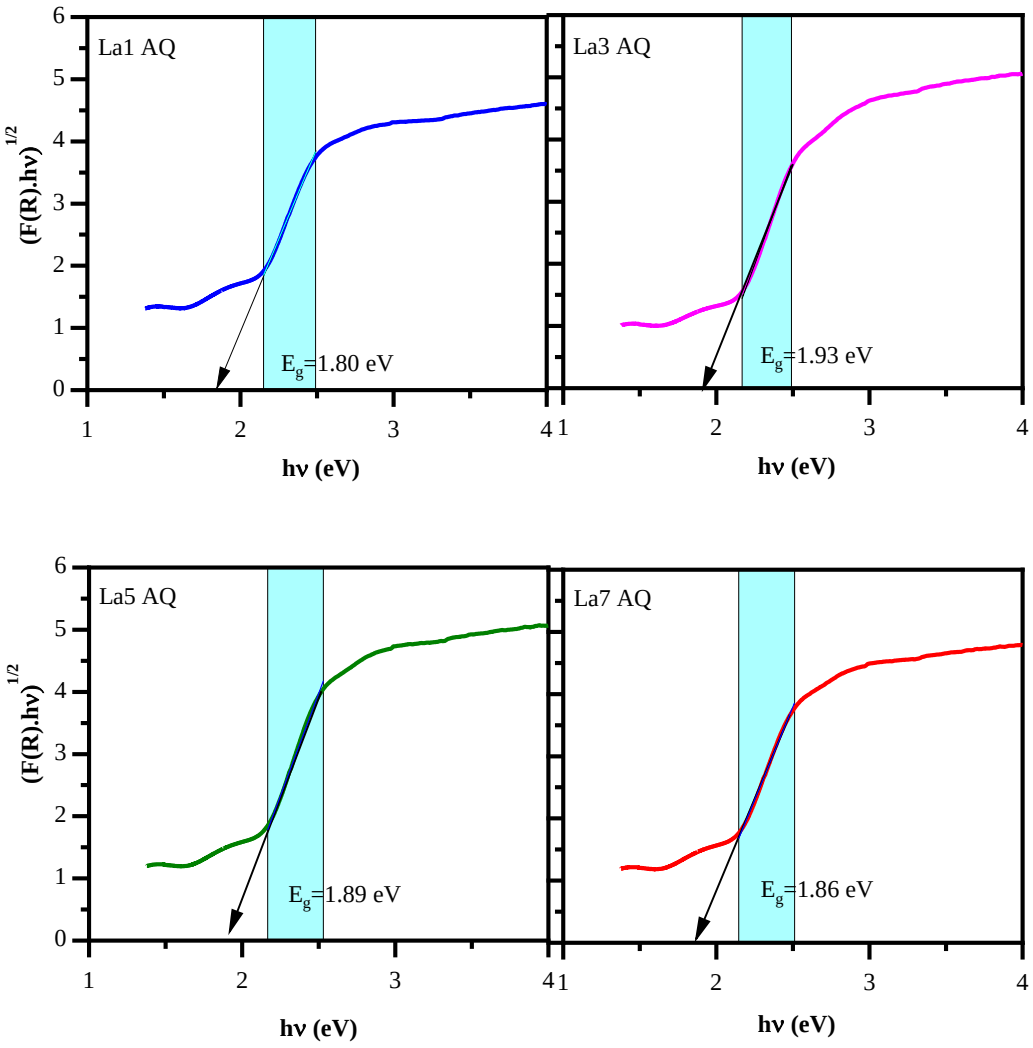


Figure 5.4 Kubelka Munk Tauc plot for BLFBT with (a) y=0.01 (La1), (b) y=0.03 (La3), (c) y=0.05 (La5), and (d) y=0.07 (La7).

Furthermore, the observed sub-bands, characterized by lower band gap values ($E_{g1}$), are indicative of defect states within the band gap, primarily arising from oxygen vacancies or impurity levels introduced by doping. These sub-bands, which absorb lower energy photons, are manifested as slight humps with smaller slopes in the lower energy region of the Kubelka-Munk Tauc plots ((see Figure 5.3 and Figure 5.4). The band gap values obtained from the

threshold in this region, referred to as $E_{g1}$, are lower than the actual optical band gap ($E_g$). Specifically, the $E_{g1}$ values are 0.68 eV (for x=0.01), 0.69 eV (x=0.03), 0.79 eV (x=0.05) and 0.63 eV (0.07) for BFSBT-x. The $E_{g1}$ values are 0.64 eV (y=0.01), 0.68 eV (y=0.03), 0.60 eV (y=0.05) and 0.51 eV (y=0.07) for BLFBT-y. Oxygen vacancies contribute to localized states in the band gap, which can trap carriers and influence both the material's ferroelectric and magnetic properties, critical for applications of $BiFeO_3$-$BaTiO_3$ solid solutions. Overall, the intricate interplay between dopant ions, the host lattice, and defect states such as oxygen vacancies leads to complex modifications in the electronic structure, detectable through spectral analysis. These findings provide insights that can be utilized to tailor the properties of these materials for specific electronic and optoelectronic applications. Thus, by choosing a suitable dopant regardless of A or B site the band gap of the system can be reduced which can be beneficial for applications in photovoltaics and optoelectronics.

### 5.3.3 Dielectric Studies

The temperature dependent dielectric constant (dielectric permittivity) and dielectric loss (tanδ) plots at 10 kHz for BFSBT-x and BLFBT-y are demonstrated in Figure 5.5. The room temperature (~31 ºC) dielectric permittivity values increase with increasing the concentration from $\varepsilon_r'$~803 for y = 0.01 to $\varepsilon_r'$~1393 for y=0.07. The similar trend was observed for Sc doping where it increased from $\varepsilon_r'$~578 to 661. A weak relaxation was observed at around 250 ºC in BLFBT-y=0.03 and at ~300 ºC for BLFBT-y=0.07. The value of temperature corresponding to maximum dielectric constant represented by $T_m$ has value ~351 ºC for BFLBT-y=0.03 which shifted to ~378 ºC for y=0.07. The maximum value of $\varepsilon_r'$ at $T_m$ for y= 0.03 was 9579 while for x= 0.03 it could not be predicted as data available was only up to 500 ºC. The maximum value of dielectric constant corresponding to $T_m$ (~378 ºC) for y= 0.07 was 24066 and at $T_m$ (~ 443 ºC) for x= 0.07 was around 7410. The trend of dielectric constant vs

temperature with doping concentration in BFSBT-x indicates that the $T_m$ must be above 500 ºC. The overall dielectric loss remains less than 1 in wide temperature range of 31 ºC to 470 ºC for BFSBT-x samples. The specific dielectric loss values (tan δ) for x=0.03 remains around 0.2 in temperature ranging from 31-380 ºC which may be attributed to better electrical stability of $Sc^{+3}$ than $Fe^{3+}$ [182]. While the dielectric loss values range from 0.23 to 0.68 in BLFBT-y=0.03 samples for temperature ranging from 31 ºC to 380 ºC. Two relaxation peaks are observed in dielectric loss vs temperature curve, one around 100 ºC and other at 300 ºC. While the trend for La7 indicates the room temperature dielectric loss value around 0.55 followed by a sharp downfall around 200 ºC reaching the value of 0.2 and on further increasing the temperature it gives a peak around 296 ºC corresponding to dielectric relaxation. The dielectric losses increase abruptly after the temperature exceeds 350 ºC in La7 and Sc7 samples. The frequency dependent dielectric constant plots for BFSBT-x=0.07 (Sc7) and BLFBT-y=0.07 (La7) are depicted in Figure 5.6. High values of dielectric constant at low frequencies could be attributed to Maxwell-Wagner type contribution. Space charge polarization related to oxygen vacancies contributes to the dielectric response at lower frequencies. As the frequency increases the value of dielectric constant decreases because of inability of dipoles to reorient themselves with the applied electric field at higher frequencies.

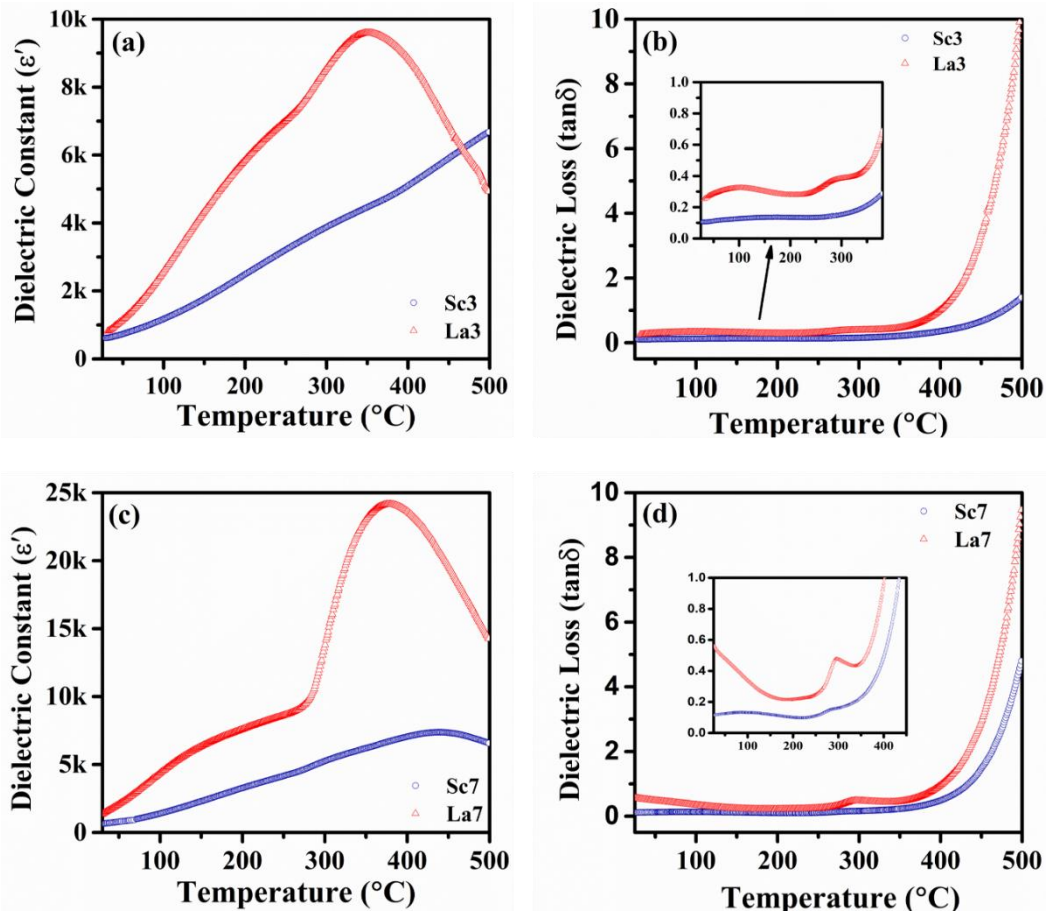


Figure 5.5 Temperature dependent (a, c) dielectric constant plot for x, y= 0.03, 0.07 and (b, d) dielectric loss plot for x, y=0.03, respectively.

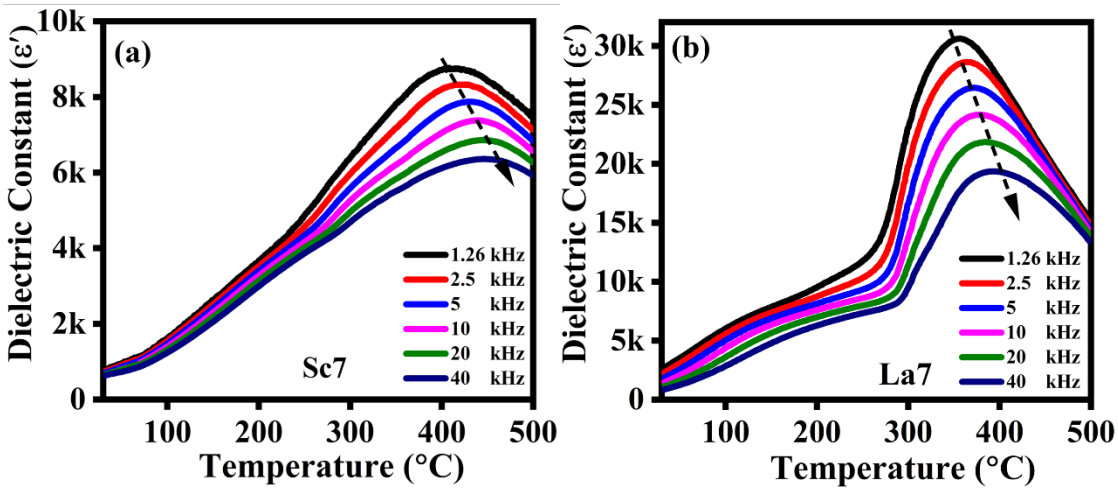


Figure 5.6 Temperature dependent dielectric constant as a function of frequency for (a) x=0.07 (Sc7) and (b) y=0.07 (La7).

At higher frequencies, the internal friction becomes more significant, leading to the dissipation of energy as heat. This dissipation reduces the ability of the material to store electric charges and hence decreases the dielectric constant. The broad frequency dependent diffused curve of dielectric permittivity indicates the relaxors-like behavior, enabling these materials to exhibit large strains and functionalities over a wide temperature range, making them valuable for actuators and transducers. This diffuseness arises from the polar nanoregions (PNRs) within the material in regions where local electric dipoles can fluctuate or reorient. The degree of diffuseness reflects the distribution of relaxation times associated with PNRs of different sizes and orientations. PNRs are crucial for understanding the unique properties of relaxor ferroelectrics. The presence of diffuseness is intimately related to the absence of a well-defined Curie temperature, as observed in traditional ferroelectric materials. Relaxor ferroelectrics often exhibit a broad temperature range over which the dielectric response is significant, allowing them to operate effectively over a wide temperature range. This diffuseness parameter can be characterized using the modified Curie-Weiss law equation as proposed by K. Uchino and Nomura.[232]

$$1/\varepsilon_r^{'} - 1/\varepsilon_m = (T - T_m)^{\gamma}/C \qquad [T > T_m] \qquad (5.4)$$

Where $\varepsilon_r'$ is real part of dielectric permittivity, $\varepsilon_m$ is the maximum value of the dielectric constant corresponding to $T_m$ and C is Curie like constant. The $\gamma$ denotes the critical exponent (degree of diffuseness) in relaxor ferroelectrics. As the temperature changes, the relaxation dynamics of the PNRs and the associated dielectric response are altered. Generally, a value close to unity represents the normal ferroelectric behavior of material while the values lying in close proximity to 2 indicate the relaxor behavior. The slope of the linear fit of the plot between ln $(1/\varepsilon_r' - 1/\varepsilon_m)$ vs ln$(T-T_m)$ gives the value of $\gamma$. The linear fit of the ln $(1/\varepsilon_r' - 1/\varepsilon_m)$ vs ln $(T-T_m)$ for BFSBT-x=0.07 (Sc7) and BLFBT-y=0.07 (La7) are given in Fig. 6. The degree of diffuseness obtained for Sc7 is around 1.65 and that for La7 is as high as 1.91 signifying the

relaxor behavior. Relaxor dielectrics exhibit complex and frequency-dependent dielectric properties, such as a broad frequency dispersion and a broad peak in the temperature-dependent dielectric response. The Vogel-Fulcher-Tammann (VFT) fitting method is widely used in the study of relaxor dielectrics because it provides insights into the temperature-dependent behavior of these materials. VFT fitting helps in characterizing the relaxor behavior by providing parameters such as the Vogel-Fulcher temperature ($T_{VF}$), activation energy ($E_a$), and pre-exponential factor ($f_o$). The VFT equation assumes that the relaxation time of the material diverges at the Vogel-Fulcher temperature ($T_{VF}$). The activation energy indicates the energy barrier for relaxation processes, and $T_{VF}$ is related to the onset of relaxation processes. At temperatures below $T_{VF}$, the relaxation time of the material becomes exceedingly long. As a result, the material's ability to promptly respond to applied electric fields or external perturbations is significantly reduced. This is often associated with the freezing of dynamic molecular or atomic motions that contribute to the relaxation processes in the material. The dielectric properties and relaxation dynamics of materials near $T_{VF}$ exhibit a strong temperature dependence. Small temperature changes can significantly affect the dielectric response and relaxation behavior of the material. This sensitivity to temperature is a distinctive feature near the Vogel-Fulcher freezing temperature. It provides insights into the transition from a highly mobile state at higher temperatures to a frozen or glassy state at lower temperatures, impacting various aspects such as electrical conductivity, polarization behavior, and energy dissipation in relaxor dielectrics. The VFT fitting was done according to the given equation: -

$$f = f_o \, e^{\left\{\frac{E_a}{k_B(T_m - T_F)}\right\}} \qquad (5.5)$$

Where f represents the measurement frequency and other variables have their respective meanings as per explanation provided. Figure 5.8 demonstrates the well fitted VFT plots for BFSBT-x=0.07 (Sc7) and BLFBT-y=0.07 (La7). The calculated activation energy from the

VFT fitting for Sc7 was around 0.05 eV while the same was 0.07 eV for La7. The VFT model accounts for freezing temperatures of ~633 K for Sc7 and of ~551 K for La7.

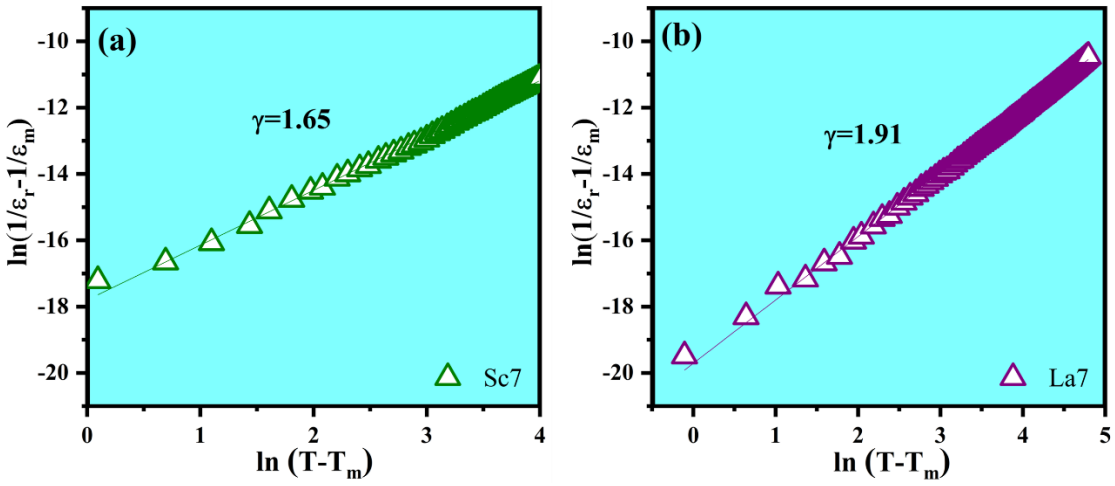


Figure 5.7 Modified Curie–Weiss law linear fitting plot of $\ln(1/\varepsilon_r - 1/\varepsilon_m)$ vs $\ln(T - T_m)$ for (a) x=007 (Sc7) and (b) y=0.07 (La7) at 10 kHz.

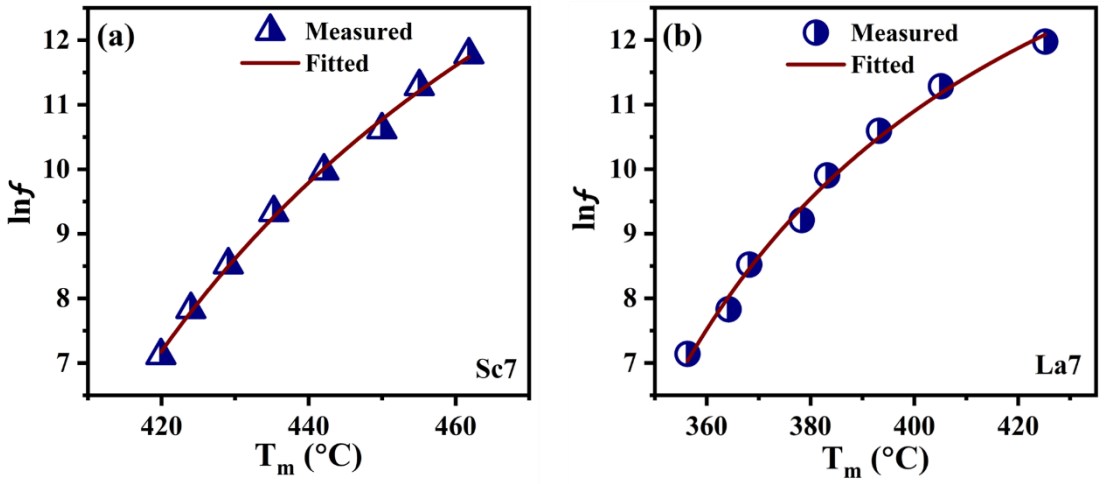


Figure 5.8 Vogel Fulcher model fitting for (a) x =0.07 (Sc7) in BSFT and (b) y= 0.07 (La7) in BLFT.

### 5.3.4 Ferroelectric Studies

Figure 5.9 (a-d) depicts the room temperature polarization vs electric field hysteresis loops of BFSBT-x and BLFBT-y ceramics samples. Figure 5.9 (e) demonstrates the associated double y axes plot between remnant polarization ($2P_r$) and coercive field ($2E_C$) which provides a comprehensive understanding of the ferroelectric properties of these materials. The P-E loops for BFSBT-x samples display robust ferroelectric characteristics with well-saturated loops, particularly notable in the x=0.03 composition where the maximum $2P_r$ value reaches approximately 21.27 $\mu C/cm^2$ and the $2E_C$ is around 49.48 kV/cm. This optimal doping level suggests a favorable alignment and density of ferroelectric domains, facilitating easy domain switching and indicating a healthy balance between enhanced polarization and manageable coercive forces. In contrast, the BLFBT-y series exhibits a progressive decrease in loop robustness, with P-E loops becoming slimmer and thinner from La1 to La7 as La concentration increases. This trend is accompanied by a reduction in remnant polarization from approximately 16.8 to 7.9 $\mu C/cm^2$ with relatively stable coercive fields around 62-65 kV/cm. The thinning of the loops and decrease in $2P_r$ values indicate a deterioration in ferroelectric properties, increasingly hampered by domain wall pinning. Domain wall pinning, exacerbated by higher doping levels, significantly affects the ferroelectric properties. The presence of defects such as oxygen vacancies, which tend to increase with doping concentration introduces local energy barriers that obstruct domain wall movement. These defects create charge imbalances and localized energy states within the crystal structure, interacting with domain walls and hindering their mobility. As a result, the P-E loops become more lossy, and the efficiency of ferroelectric switching decreases, necessitating higher electric fields to achieve polarization reversal. This is evident in the relatively stable, yet high coercive field values observed in the BLFBT-y series, reflecting the material's increased resistance to polarization switching despite the adverse impact of defects and pinning [230].

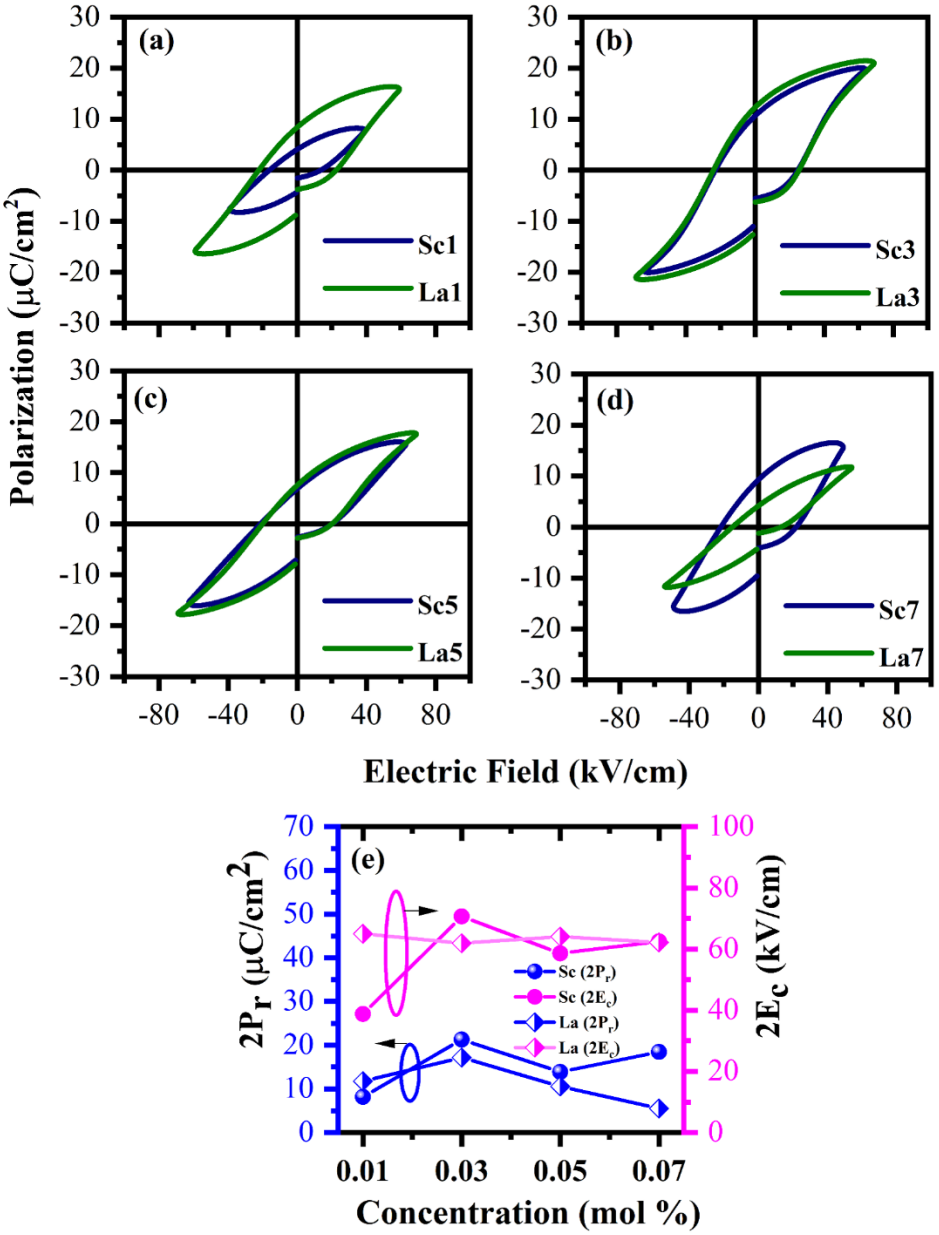


Figure 5.9 Ferroelectric hysteresis loops for (a) x, y=0.01 (b) x, y=0.03 (c) x, y=0.05 and (d) x, y=0.07 in BFSBT-x and BLFBT-y.

Furthermore, the energy storage density of relaxor dielectrics was investigated using ferroelectric hysteresis loop for estimating the area under the charge /discharge cure and polarization axis using following relations:

$$W_{rec} = \int_{P_r}^{P_{max}} EdP, \qquad (5.6)$$

$$W_{Total} = \int_{0}^{P_{max}} EdP \text{ and,} \qquad (5.7)$$

$$\eta\ (\%) = (W_{rec}/W_{Total}) * 100, , \qquad (5.8)$$

where $W_{rec}$ is recoverable energy storage density while $W_{Total}$ is total energy storage density, η is efficiency, $P_r$ is remnant polarization, $P_{max}$ is maximum polarization and E is applied electric field [247].

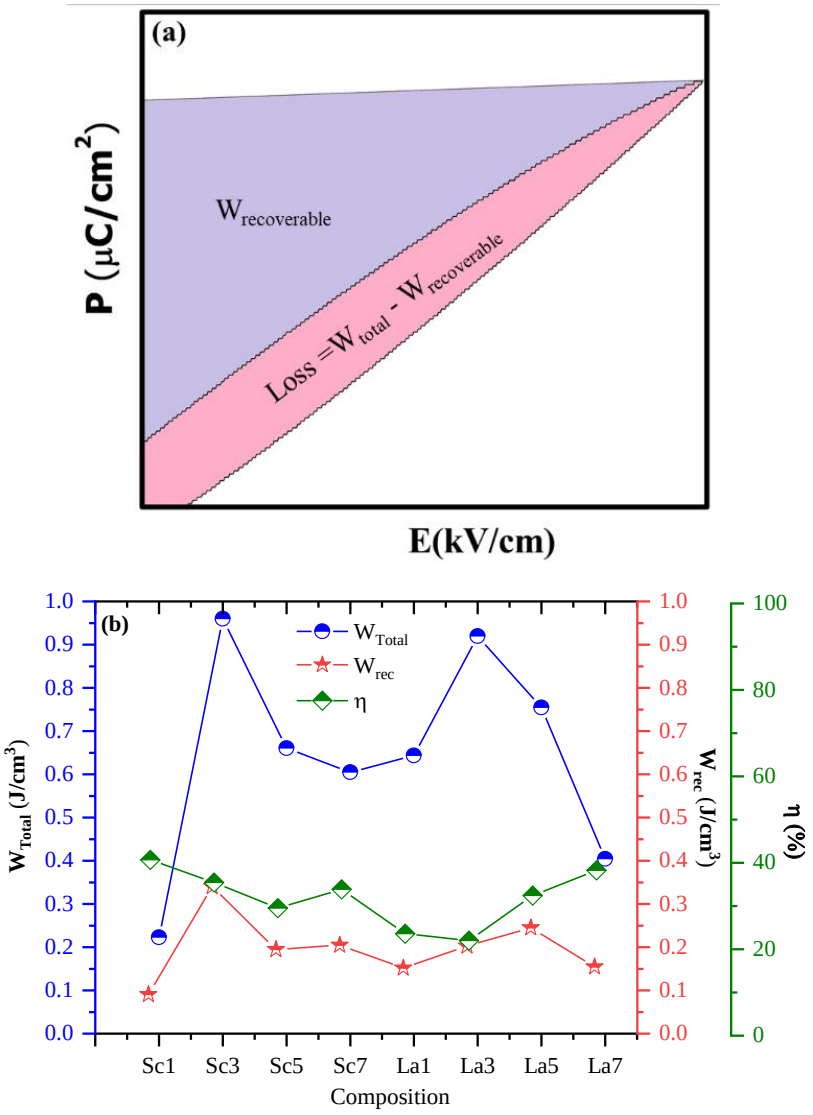


Figure 5.10 (a) P-E hysteresis loop depicting energy storage density calculation, and (b) Comparison of $W_{Total}$, $W_{rec}$ and η for different compositions of BFSBT-x and BLFBT-y.

For BFSBT-x compositions, the highest efficiency was observed at x = 0.01 (Sc1) with $W_{rec}$ ~ 0.09 J/cm$^3$ and η ~ 40.54 %. As the doping concentration increased, the efficiency declined, reaching its lowest at x = 0.05 (Sc5) with $W_{rec}$ ~ 0.194 J/cm$^3$ and η ~ 29.39 %. In contrast,

BLFBT-y compositions showed an increasing efficiency trend with higher doping levels, peaking at y = 0.07 (La7) with $W_{rec}$ ~ 0.154 J/cm$^3$ and η ~ 38 %. These findings underscore the significant impact of doping concentration on the energy storage efficiency of these materials.

Despite their potential, the recoverable energy storage densities $W_{rec}$ for modified $BiFeO_3$-based relaxor ferroelectric ceramics are relatively low, primarily due to the limited permissible electric field. This is significantly less than that of other extensively researched lead-free perovskite ceramics such as those based on $NaNbO_3$, BNT, BT, and $AgNbO_3$[248] . The breakdown field $E_B$ is a vital parameter for energy storage dielectrics, as it determines the maximum applied voltage. It is influenced by intrinsic factors like dielectric constant, band gap, density, defects, grain size, and grain boundaries, as well as extrinsic factors including sample area, thickness, electrode configuration, temperature, humidity, voltage type, and test duration.

$BiFeO_3$-based compositions typically exhibit lower band gaps and higher dielectric losses and conductivities, mainly due to the volatilization of Bi and the reduction of $Fe^{3+}$ during the sintering process. To address these issues, the breakdown field can be enhanced by incorporating multivalent elements and using them as sintering aids, or by developing thin films. These thin film forms, which can achieve higher breakdown strengths, show great promise for enhancing $W_{rec}$, thus making them highly suitable for large-scale industrial applications in capacitive energy storage devices. In conclusion, the energy storage performance of BFSBT and BLFBT compositions shows significant variability with doping concentration. While the observed efficiencies are relatively high, further improvements in are achievable by optimizing the material composition and processing conditions, especially in thin film forms. Future research should focus on overcoming the limitations posed by low breakdown fields and exploring new doping strategies to enhance the energy storage capabilities of these promising materials.

## 5.4 Conclusion

The BFST and BLFT ceramics have been successfully synthesized by solid state route (SSR) utilizing air quenching. All samples have pure perovskite structure along with pseudocubic phase as the major phase. The $La^{+3}$ doping helps in pure phase formation while $Sc^{+3}$ doping helps in increasing the resistivity and ferroelectric behavior. The room temperature dielectric constant has increased from 578 to 661 for BFST and 803 to 1393 for BLFT with increasing doping concentration from 1 to 7 mol%. The temperature dependent dielectric constant curves show broad frequency dependent peaks which indicates the relaxor like behavior which was further confirmed by modified Curie-Weiss law fitting giving the value of diffusivity constant close to 2. From the calculation of energy storage density, the maximum $W_{rec}$ value of ~ 0.34 J/cm$^3$ for x=0.03 and ~ 0.25 J/cm$^3$ for y=0.05 were obtained. Irrespective of the doping site the optical band gap has reduced (~1.8 eV) with respect to pure BFO and BT, which can be beneficial for photovoltaics and optoelectronics applications. In conclusion, this chapter underscores the delicate interplay between dopant type, concentration, and the resulting material properties in BFSBT-x and BLFBT-y ceramics. Optimizing doping strategies using site engineering is crucial for enhancing the material's polarization capabilities while mitigating the negative effects of domain wall pinning and defect formation. A deeper understanding of these microscopic interactions can guide the development of materials with tailored ferroelectric properties, enhancing their application potential in technology.